"ARIANE 5" TPLOX INDUCER DESIGN STRATEGIES TO ENHANCE CAVITATING PERFORMANCE

A. Arnone, P. Boncinelli
"Sergio Stecco" Department of Energy Engineering
University of Florence – Florence, Italy

A. Capuani, E. Spano
FIAT Avio S.p.A. – Cryogenic Turbopump Division
Turin, Italy

C. Rebattet
CREMHyG – Centre de Recherches et Essais de Machines Hydrauliques de Grenoble
Grenoble, France

Abstract

Optimization process in cavitating conditions of the axial inducer of the *"Ariane 5"* main engine liquid oxygen (LOX) turbopump is described in details. Different inducer configurations were set up and investigated, starting from the reference one to produce an optimized final geometry. Both 3D fully–viscous computations and experimental tests in water and LOX were exploited during this activity. Computations allowed the designer to identify cavitation inception on the reference inducer, and to compare its performance to the final one, assessing the effectiveness of the redesign process. Experiments were carried out to study the development of cavitation, investigate the inducer behavior in cavitating conditions, and suggest suitable modifications to the geometry. As a result, an optimized blade leading edge shape was set, which revealed a significant trend to reduce cavitation effects with a good smoothing of the head/cavitation curve.

Nomenclature

$\dot{m}$	mass flow	Ω	angular velocity
$\dot{m}_n$	nominal mass flow	ν_n	rotating frequency
p	static pressure	$Z = 4$	number of inducer blades
p_{01}	averaged inlet total pressure	$\phi \equiv \frac{\dot{m}}{\rho\Omega}$	flow coefficient
p_v	vapor pressure	$\psi \equiv \frac{\Delta p_0}{\rho\Omega^2}$	total pressure rise coefficient
Δp_0	total pressure variation	$\tau \equiv \frac{NPSP}{\rho\Omega^2}$	cavitation coefficient
$NPSP = p_{01} - p_v$	Net Positive Suction Pressure		
ρ	density		
Re	Reynolds number		

1 Introduction

Nowadays, the huge expansion of space activities for scientific and commercial purposes has made cheaper payload lift capability as one of the most interesting features of the new–generation launchers. Actually, its increase is perhaps the most important tasks to be fulfilled during the design process of the whole rocket, and the competition between different manufacturers develops mainly on this level. The complete redesign of the *"Vulcain"* main engine of the *"Ariane 5"* European rocket fits into this context, including turbopump for the Liquid Oxygen (LOX) propellant, which was designed, built and tested by FIAT Avio.

The need of weight reduction in a launcher usually implies the requirement that turbopumps operate at very low inlet pressure. In this condition, cavitation phenomena often occur at the first component inlet. To reduce cavitation risks on the centrifugal impeller, which provides most of the pump head, an axial inducer is usually put before it, as in the *"Vulcain"* and *"Vulcain 2"* turbopumps.

One of the crucial point in the inducer design is the fulfillment of NPSP requirements at the inlet. Cavitation can be tolerated if good suction behavior, good head rise, low radial loads and vibration levels can still be achieved. Consequently, the designer is interested in having effective tools at disposal to study the development of cavitation, and its impact on the component's performance.

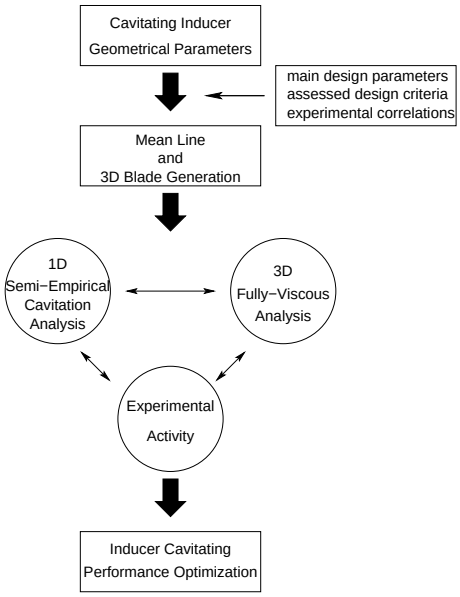

Figure 1: Scheme of the inducer optimization process.

Many authors have worked on this problem [1, 2, 3]. In the last decade, FIAT Avio has paid special efforts to improve the inducer design in terms of suction performance, dynamic stability and inducer rotating cavitation, which leads to very high radial loads (see [4]). The establishment of a closer cooperation with academic institutions, such as the "Sergio Stecco" Department of Energy Engineering of the University of Florence, and the "Centre de Recherche et d'Essais de Machines Hydraulique de Grenoble (CREMHyG)", allowed FIAT Avio designers to exploit some of the most up–to–date CFD and experimental tools to achieve an optimized inducer configuration.

In this work, design strategies adopted during the optimization process and the engineering approach used to reach this target are presented. Main phases are summarized in fig. 1. The design process began by fixing the main inducer geometrical parameters: tip diameter, blade angle at leading edge, inlet flow angle, leading edge shape, casing contouring, blade thickness and solidity. A 3D preliminary design of the blade was then accomplished by means of 1D numerical techniques, according to all the assessed design criteria and experimental correlations collected in the past. A first check on the behavior in cavitating conditions was done by means of a semi–empirical 1D code, owned by FIAT Avio. Then, 3D fully–viscous computations were performed on this reference inducer in non–cavitating conditions, in order to assess its performance in the pump flight envelope, and explore flow structure details. An analysis of cavitation inception was carried out on the basis of CFD results, too. Finally, after manufacturing the component, experimental tests were set up to investigate details of the cavitation development, and its impact on the performance. This experimental activity consisted of three subsequent steps:

1. the axial stage characterization in water, carried out at the CREMHyG test rig;
2. the complete full–scale pump characterization in water, carried out at the FIAT Avio test rig in Colleferro;
3. the complete full–scale pump characterization in LOX, carried out at the ASTRIUM DASA P59 test rig in Octobrunn.

During the first step, two different inducer configurations were tested: the reference inducer (fig. 2(a)), and a remachined inducer, obtained by changing the blade leading edge tip (fig. 2(b)). All static and dynamic experimental data were used to improve the inducer performance by modifying directly its geometrical parameters. As a result, a final inducer configuration was set up with an optimized leading edge shape (fig. 2(c)). Its performance was assessed during the last two experimental campaigns both in water and in LOX, and by means of 3D computations.

2 CFD Analysis

Nowadays, CFD techniques are commonly used in the aerodynamic design of industrial turbomachine components. Unfortunately, without a suitable numerical model, it is not possible to solve directly cavitating flows: this would lead to compute negative static pressures in some cells of the domain, making it impossible to perform calculations. Moreover, the phenomenon is typically unsteady and non-axisymmetric, requiring considerable computational resources. Basic research on cavitation models is still in its developing phase, and applications to everyday industrial design seem far to be achieved. However, 3D computations can still be used to identify cavitation inception, even if details of its development cannot be provided. It is also possible to compare different geometries to find out which is expected to give the best performance in cavitating conditions.

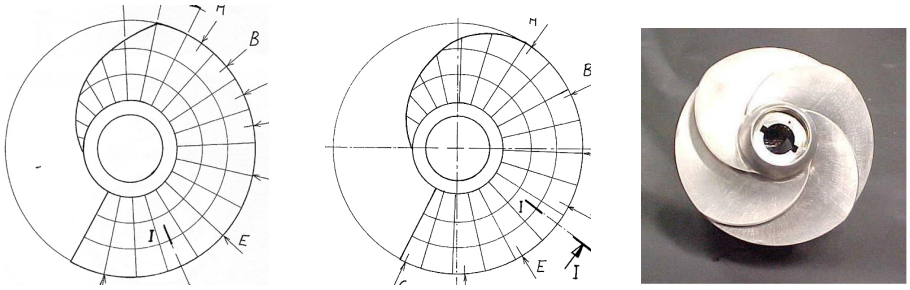

(a) Reference inducer geometry.

(b) Remachined inducer geometry.

(c) Final inducer view.

Figure 2: Examined inducer configurations.

2.1 Numerical Procedure

CFD results for the *"Vulcain 2"* inducer were obtained using the HYDRO code, a fully viscous, multigrid, multi-row solver developed by the University of Florence, capable of solving 3D cascade flows in coupled fixed and rotating blade passages using non–periodic H–type or C–type grids. The concepts of artificial compressibility of Chorin [5] are used to handle incompressible fluids by a time–marching approach. The eddy–viscosity hypothesis is used to account for the effect of turbulence. The eddy viscosity is computed using the two–layer mixing length algebraic model of Baldwin and Lomax [6].

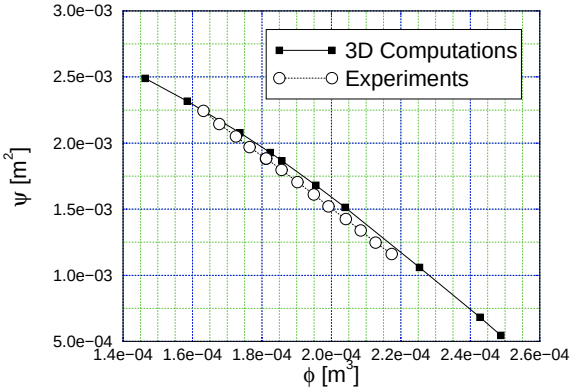

Figure 3: Reference inducer computed and measured performance.

The 3D unsteady incompressible Reynolds–averaged Navier–Stokes (RANS) equations are discretized in space using a a cell–centered finite volume scheme. The solution is advanced in time using an explicit four–stage Runge–Kutta scheme, until the steady state solution is reached. In order to reduce the computational cost and speed up convergence to the steady solution, four computational techniques are employed (local time–stepping, residual smoothing, multigrid FAS scheme and grid refinement). Further details on the numerical procedure can be found in [7, 8, 9, 10, 11].

A non–periodic H–type grid was employed, with $169 \times 49 \times 49$ grid points along the streamwise, blade–to–blade and spanwise directions respectively.

In all computations the evolving fluids (water and LOX) were considered incompressible and isothermal. Due to the high values of the Reynolds number (from $Re \simeq 10^7$ up to 10^9), a fully–turbulent boundary layer was assumed on both blade and end-wall surfaces in all computations. An average value of $y^+ = 10$ was accepted on the basis of comparisons between experiments and computations on the *"Vulcain"* inducer performance [11].

2.2 Results

3D fully–viscous computations were performed to characterize the *"Vulcain 2"* reference inducer behavior both at design point and in off-design conditions, both in LOX and in water. The computed performance in water was found to get along well with experimental measurements in non–cavitating conditions ($\tau = 6.7 \cdot 10^{-4}$). Results are summarized in fig. 3, where the corresponding $\psi - \phi$ curves are reported.

To deal with cavitation, such an approach was followed. The flow was pressurized to some extent respect to physical pressure in the tanks, preventing cavitation from arising, and computations were performed. Then, the added level of pressurization was subtracted from the computed values of static pressure on the inducer blade. This allowed

the designer to find out which portions of the blade were likely to be be affected by cavitation by looking for negative values of static pressure, neglecting LOX vapor pressure compared with inlet total pressure p_{01}.

Such an analysis was carried out for two different operating points of the reference inducer, at 100% and 120% of the nominal mass flow rate. In fig. 4(a)–4(d) nondimensional static pressure distributions on the inducer blade are reported as a function of the relative curvilinear abscissa at 10%, 50% and 90% of the blade span. The value of zero pressure has been marked for reference. Figures 4(b)–4(e) highlight negative static pressure regions on the inducer blade at the same operative points, allowing one to compare them with experimental visualizations (fig. 4(c)–4(f)). No cavitation is seen to develop either near blade hub or at midspan. Blade load near leading edge is quite low for all the two points. Cavitation inception is present near tip, where a deep minimum of static pressure, well below zero, is observed on the blade suction side. Both the absolute value of such a minimum and the percentage of the affected blade length increase while lowering the mass flow rate. The development of cavitation is helped also by positive incidence of the flow near blade tip, as it can be clearly seen by the peak of pressure on the pressure side, which considerably increases the blade load, and, consequently, the local acceleration around leading edge.

Computations were also performed on the final inducer configuration, whose blade tip geometry had been modified following suggestions coming from numerical and experimental tests, presented later on. Results for three different operating points (about 120%, 100% and 90% of the nominal flow rate $\dot{m}_n$) are shown in fig. 5. A decrease in the pressure minimum value is observed, compared with the reference configuration, especially at the design point (fig. 5(a)–5(b)–5(c)). Such a result, together with experimental tests in water and LOX, allowed the designer to assess the effectiveness of the redesign process.

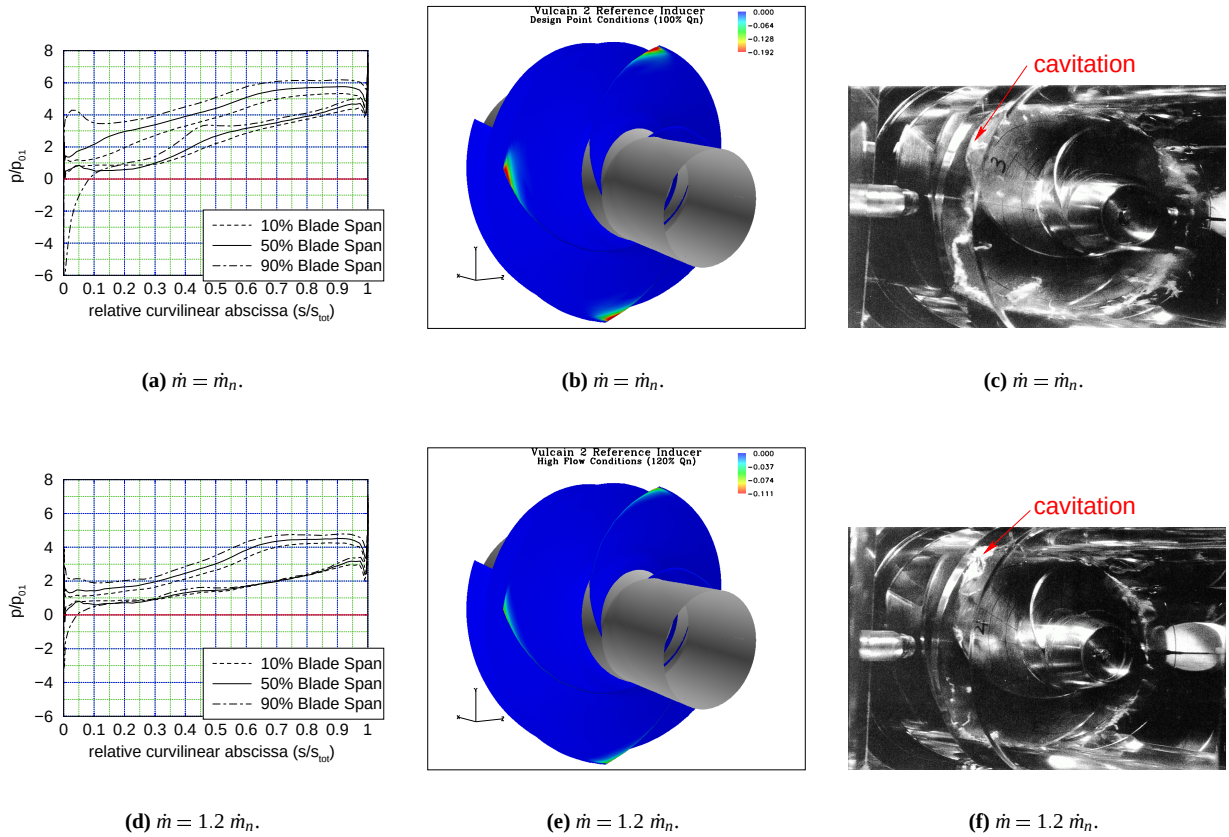

(a) $\dot{m} = \dot{m}_n$. **(b)** $\dot{m} = \dot{m}_n$. **(c)** $\dot{m} = \dot{m}_n$.

(d) $\dot{m} = 1.2\ \dot{m}_n$. **(e)** $\dot{m} = 1.2\ \dot{m}_n$. **(f)** $\dot{m} = 1.2\ \dot{m}_n$.

Figure 4: Static pressure distributions on blade (left), computed blade regions of cavitation inception (center) and experimental visualizations in water (right) for the reference inducer configuration.

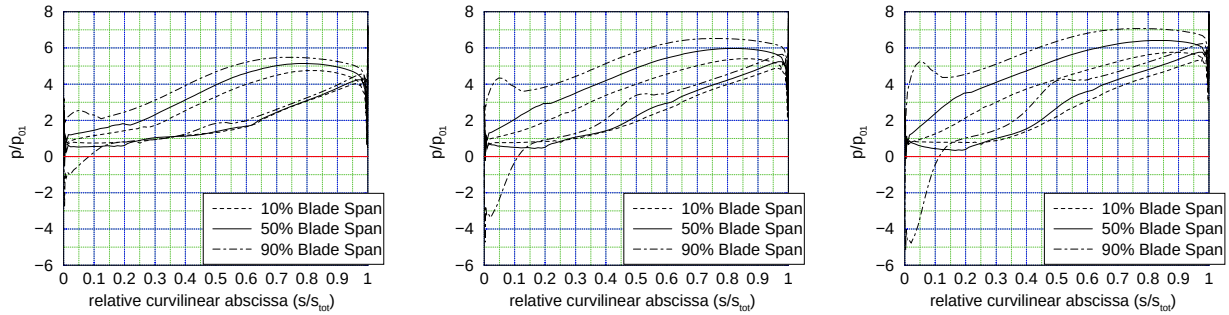

(a) $\dot{m} = 1.2\ \dot{m}_n$. **(b)** $\dot{m} = \dot{m}_n$. **(c)** $\dot{m} = 0.9\ \dot{m}_n$.

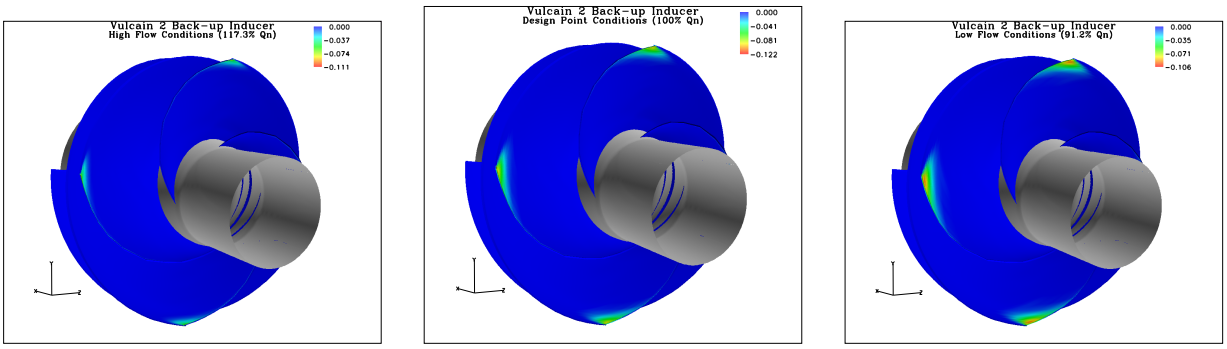

(d) $\dot{m} = 1.2\ \dot{m}_n$. **(e)** $\dot{m} = \dot{m}_n$. **(f)** $\dot{m} = 0.9\ \dot{m}_n$.

Figure 5: Static pressure distributions on blade (above) and computed blade regions of cavitation inception (below) for the final inducer configuration.

3 Water Tests in Cavitating Condition

The development of cavitation and its effects on the inducer performance at different operating conditions were studied by means of experimental campaigns, which were carried out both in water and in LOX. The main results of this activity are presented here.

3.1 Experimental Setup

Tests in water on the reference inducer were performed at the TM2 rig of CREMHyG laboratory (fig. 6(a)), and at FIAT Avio test facility in Colleferro (6(b)). The first one was devoted to the axial stage characterization, the second one to the complete pump. Both of them have a rotational speed of 6000 RPM. On the CREMHyG rig, a transparent liner equipped with dynamic pressure transducers allows one to observe cavitation pattern development while decreasing the cavitation coefficient τ. To analyse the interaction between the cavitating pump and the circuit, an accumulator is located at the inlet: this apparatus fixes the resonant frequency at inlet value and makes easier to compare tests for incipient surge cavitation.

Two different sequences of data are achieved for different operating points. The first one is the classical point by point procedure at a constant flow rate condition in order to investigate the breakdown cavitating performance and to take visualizations through the liner. The second one proceeds at a given flow rate with continuous decreasing of inlet pressure from absence of cavitation to a head loss of 20%, corresponding to an overall loss of 5% of the pump. A cartography of regimes as functions of τ is obtained from each dynamic measurement: vibrations, loads on shaft, pressure and so on. Some pictures of cavitation patterns and spectral analysis of wall pressure values on liner upstream the leading edge are presented here.

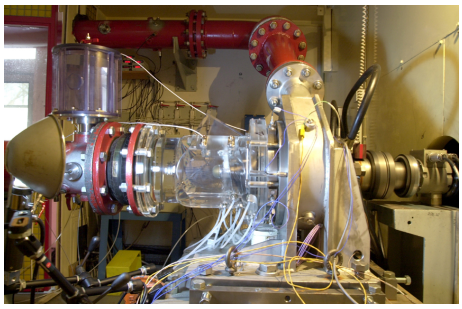

(a) CREMHyG test rig (H_2O).

(b) Colleferro test rig (H_2O).

Figure 6: Experimental facilities in water.

3.2 Test Rig and Inducer Configurations

Two different inducer configurations were tested at CREMHyG to experiment impact of the design on the cavitating instabilities. The first one consisted of the full scale inducer and a liner at nominal tip clearance size (see front view in fig. 2(a)). Then, a modification to the inducer leading edge design near tip was proposed, and the remachined inducer tested with the nominal liner (fig. 2(b)).

A final configuration (*"final inducer"*) with an optimized logarithmic leading edge shape was tested at Colleferro closed–loop rig during the complete full–scale pump characterization in water (fig. 2(c)).

3.3 Cavitating Flow Conditions

The inducer performance is strongly affected by cavitation. As already observed in 3D numerical results, cavitation develops mainly in front of blade leading edge at tip. Consequently, some changes to the blade and the shroud geometry are suggested in order to modify the interaction between the flow and the blade when the extension of cavities increases while lowering the cavitation number τ. In the circumferential region, a backflow cavitation occurs at low flow rates, which mainly depends on the choice of inlet blade angle and tip clearance size. A considerable fraction of the the volume of vapor is distributed circumferentially, and auto–oscillation is observed, even if the head rise is not affected. At low values of τ, another type of surge appears with strong axial pulsation of pressure and flow rate in the pumping system. All these hydroacoustical excitations may damage the circuit. Another important effect is the onset of radial loads induced by rotating cavitation. These phenomena have been observed in other experiments (see [12, 13]), and usually occur at flow rates for which the slope of the ψ/τ characteristic becomes discontinuous, oscillating between negative and positive values, just before the drop at breakdown.

Rotating cavitation is characterized by a circumferentially propagating phenomenon at leading edge tip, whose frequency value is slightly larger or smaller than the rotational one ν_n. 2D models and unsteady cavitating CFD are consistent to demonstrate the importance of the unsteady distribution of flow and vapor cavities in the blade cascade [14, 15].

An important effect of the circumferentially–asymmetric vapor patterns is the induced hydraulic unbalancing effect, which generates radial loads on the shaft, and, consequently, may cause a mechanical damage on the rotor arrangement (see [16]).

3.4 Results

Such flow behaviors were well observed during the experiments on the *"Vulcain 2"* inducer. For each of the two inducer configurations, three different flow rates were investigated: the nominal flow rate $\dot{m}_n$, $\dot{m} = 0.9\ \dot{m}_n$ and $\dot{m} = 1.1\ \dot{m}_n$. Results are presented in terms of cavitating and non cavitating performance curves, cavitation visualizations, and cartography of spectral waterfall (cascade) of inlet pressure.

The head/flow performance curve relative to the reference inducer is presented in fig. 3. The slope of the ψ/ϕ curve is negative without deviation, and the operating range is typically stable.

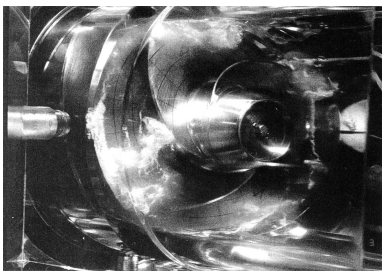

(a) V1: $\dot{m} = 0.9\,\dot{m}_n$; $\psi = 2.1 \cdot 10^{-3}$; $\tau = 6.7 \cdot 10^{-4}$.

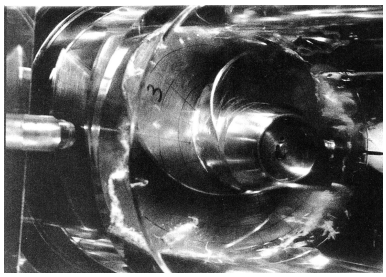

(b) V2: $\dot{m} = \dot{m}_n$; $\psi = 1.8 \cdot 10^{-3}$; $\tau = 6.7 \cdot 10^{-4}$.

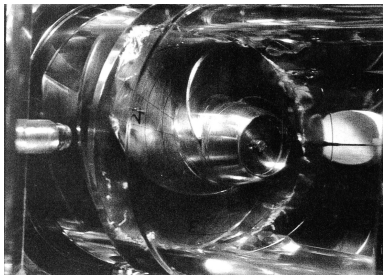

(c) V3: $\dot{m} = 1.1\,\dot{m}_n$; $\psi = 1.5 \cdot 10^{-3}$; $\tau = 6.7 \cdot 10^{-4}$.

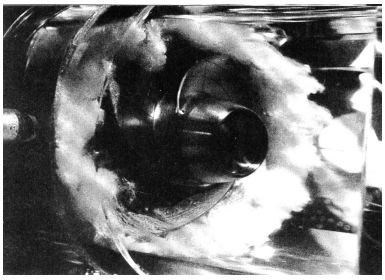

(d) V4: $\dot{m} = 0.9\,\dot{m}_n$; $\psi = 2.1 \cdot 10^{-3}$; $\tau = 1.6 \cdot 10^{-4}$.

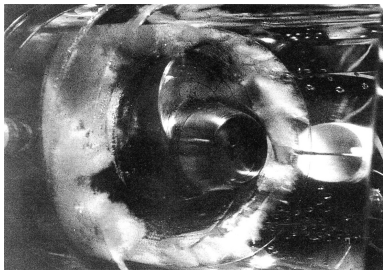

(e) V5: $\dot{m} = \dot{m}_n$; $\psi = 1.8 \cdot 10^{-3}$; $\tau = 1.6 \cdot 10^{-4}$.

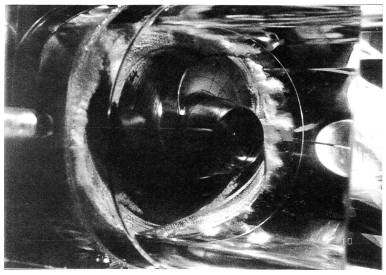

(f) V6: $\dot{m} = 1.1\,\dot{m}_n$; $\psi = 1.5 \cdot 10^{-3}$; $\tau = 1.4 \cdot 10^{-4}$.

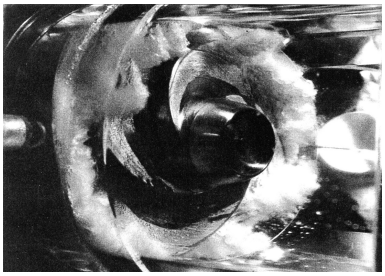

(g) V7: $\dot{m} = 0.9\,\dot{m}_n$; $\psi = 2.1 \cdot 10^{-3}$; $\tau = 1.1 \cdot 10^{-4}$.

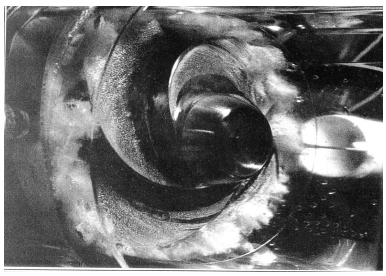

(h) V8: $\dot{m} = \dot{m}_n$; $\psi = 1.8 \cdot 10^{-3}$; $\tau = 0.95 \cdot 10^{-4}$.

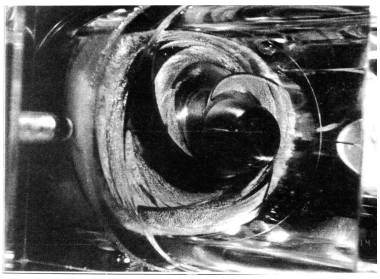

(i) V9: $\dot{m} = 1.1\,\dot{m}_n$; $\psi = 1.5 \cdot 10^{-3}$; $\tau = 1.0 \cdot 10^{-4}$.

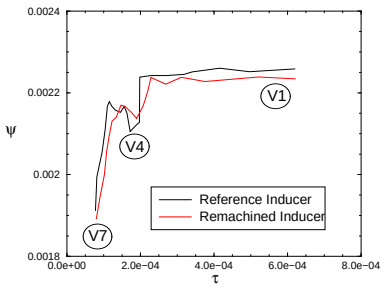

(j) $\dot{m} = 0.9\,\dot{m}_n$.

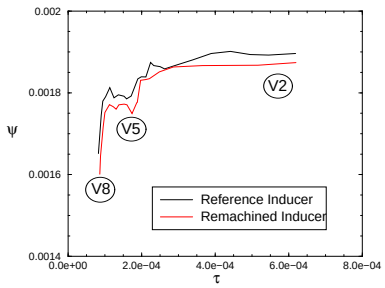

(k) $\dot{m} = \dot{m}_n$.

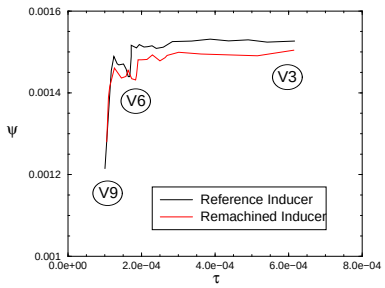

(l) $\dot{m} = 1.1\,\dot{m}_n$.

Figure 7: Experimental visualizations in water at different mass flow rates and cavitation numbers τ (above). Comparisons between the breakdown curves ψ/τ of the two different configurations at different mass flow rates (below).

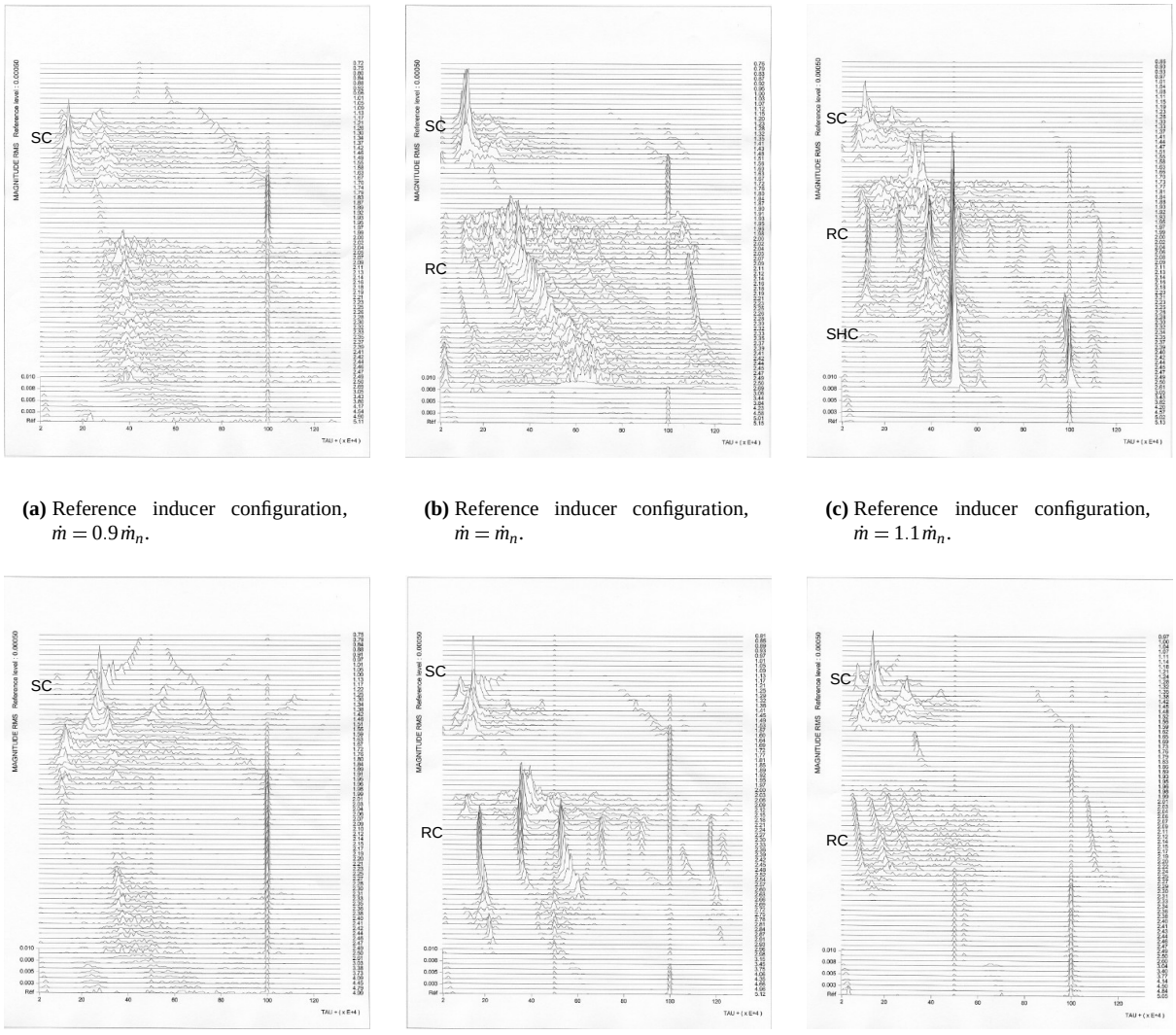

(a) Reference inducer configuration, $\dot{m} = 0.9\dot{m}_n$.

(b) Reference inducer configuration, $\dot{m} = \dot{m}_n$.

(c) Reference inducer configuration, $\dot{m} = 1.1\dot{m}_n$.

(d) Remachined inducer configuration, $\dot{m} = 0.9\dot{m}_n$.

(e) Remachined inducer configuration, $\dot{m} = \dot{m}_n$.

(f) Remachined inducer configuration, $\dot{m} = 1.1\dot{m}_n$.

Figure 8: Spectral waterfall of pressure signal at inlet as a function of the cavitation number τ at three different mass flow rates for the two configurations examined.

In fig. 7(j), 7(k) and 7(l) the ψ/τ curves are reported for the three examined flow rates, comparing the two different configurations. In cavitating conditions, the slope of the curve depends strongly on the value of ϕ and on design solutions. When the slope is positive, far from the drop, rotating cavitation occurs. When the slope becomes negative, surge cavitation and typical oscillations at low frequency are observed. Effects of the modifications on the design are clear. Visualizations taken during water tests are presented in fig. 7(a) to 7(i), for different values of ϕ, ψ and τ.

At low flow rate, backflow cavitation may oscillate with the air capacity of the accumulator located at the inlet pipe. At nominal and high flow rates, backflow disappears, while unsteady flow distribution does not still come up. For what concerns auto oscillation in the circuit, the resonant frequency at inlet was identified by means of an acoustic model, and depends on both the compressible volumes of cavitation vapor and the accumulator air capacity. These compressible volumes increase unequally while decreasing NPSP continuously, and the measured resonant frequency is a bit shifted towards lower values. Spectral cascades, presented in fig. 8 for the two inducer configurations at

Cavitation Regime	Label	Typical Frequency	Comment
Rotating Cavitation	RC	$\nu = 1.2$ to 1.0 ν_n with harmonic modulations at $(\nu - \nu_n) \cdot k$ $(k = 1, 2, \ldots)$	Circumferential propagation at LE of vapor and non equilibrium of flow through blade cascade
Surge Mode Cavitation	SC	$\nu = \nu_n/4$ and $\nu_n/10$ (acoustic resonance)	Axial excitation of system by vapor structure with accumulator or inlet pipe
Sub–Harmonic of Asymmetric Cavitation Mode	SHC	$\nu = k \cdot \nu_n/Z$ $(k = 2,\ Z = 4)$	Asymmetric patterns of attached cavities on blades or backflow cells

Table 1: Main characteristics of the observed cavitation regimes.

different operating points, focus on the low frequency domain: rotating cavitation, cavitation in backflow vortices and surge mode oscillation can be observed. Labels help one to identify the different cavitation regimes, which are presented and commented in table 1. A complete description of such phenomena can also be found in [17], with similar cascade plots of the LE–7 LOX inducer experiments using also the inlet pressure fluctuations as reference measurement.

For each design configuration and flow rate, the maximum pressure fluctuation magnitude is fixed at 1000 *Pa* on the *y* axis. The absolute magnitude of the rms pressure fluctuation is not significant, since it depends depends strongly on the axial location of the transducer. Spectral cascade axis is related to the decrease of the cavitation parameter up to the drop. On the *x* axis, frequency is reported raging from 2 *Hz* up to 1.3 ν_n. The flush mounted transducer is located between the accumulator and the inducer to magnify the axial oscillation sensitivity. The rotating cavitation is a more local oscillating phenomenon, with a stronger dependency on the axial location of the probe. However, a too much close measurement at LE to capture information on blade cascade interaction affects backflow and surge characterizations because of the upstream extension of vapor.

Both at 100% and 110% of the design flow rate, the reference inducer is affected by asymmetric, rotating and surge cavitation. Both circuit resonance and radial loads may be generated. Considering the remachined inducer, a significant attenuation is observed only at $\dot{m} = 1.1\ \dot{m}_n$, and rotating cavitation is still present. As a conclusion, the proposed remachined inducer was not efficient to avoid rotating cavitation.

4 LOX Tests in Cavitating Condition

Optimization of the inducer leading edge design produced the final inducer configuration, which was tested in water at Colleferro, and in LOX at at DASA P59 test facility in Octobrunn (fig. 9(a)). During the LOX experimental campaign, the complete turbopump was studied both in cold and hot gas turbine conditions by using the *"Vulcain"* gas generator. The rotational speed of the test rig was 12300 RPM. In the nominal configuration, the pump draws LOX. However, in experimental tests, it was necessary to use Liquid Nitrogen (LN2) instead of LOX, in order to avoid risks of explosion due to the O2/N2 mixture and the impact on walls in a high pressure LOX environment.

Cavitating performance was investigated by means of depressurization of the flow at the inducer mouth. A comparison between the inducer breakdown coefficient in water and LOX is presented in fig. 9(b) at $\dot{m} = \dot{m}_n$. Both ψ and τ coefficients are scaled using the corresponding values at the pressurized operating condition. A smoothing effect on the slope of the ψ/τ curve was observed compared to the previous inducer configurations tested at CREMHyG. Moreover, Thermal Suppression Head (TSH) was obtained, providing about 25% of gain in the operative range with respect to water breakdown condition.

Inlet pressure dynamic behaviors in water also show how supersyncronous rotating cavitation almost disappears in the final inducer configuration (fig. 9(d)) compared to the reference one (fig. 9(c)).

As a result, the final inducer configuration revealed a significant trend to reduce rotating cavitation effects with a good smoothing of the ψ/τ curve.

5 Conclusions

Design strategies adopted during the optimization process of the *"Vulcain 2"* inducer cavitating performance were presented. CFD techniques, experimental activity and mathematical modeling on the basis of assessed experience

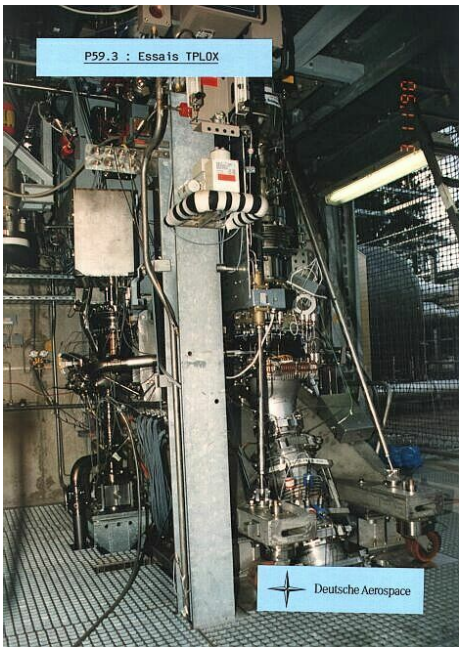

(a) DASA test rig (LOX).

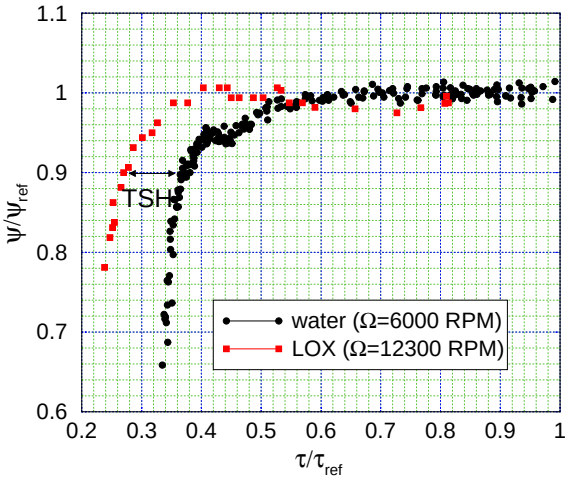

(b) Breakdown curves ψ/τ in water and LOX for the final inducer configuration ($\dot{m} = \dot{m}_n$).

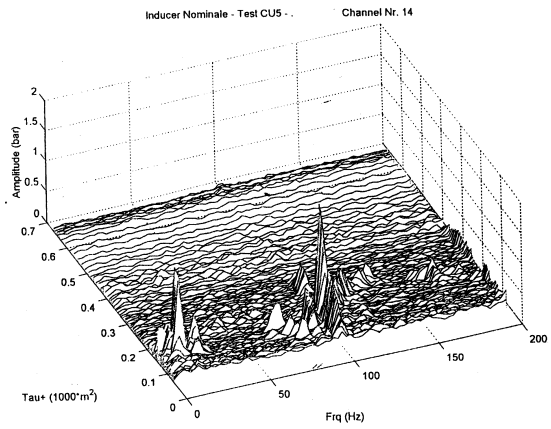

(c) Spectral pressure signal distribution for the reference inducer configuration in water ($\dot{m} = \dot{m}_n$).

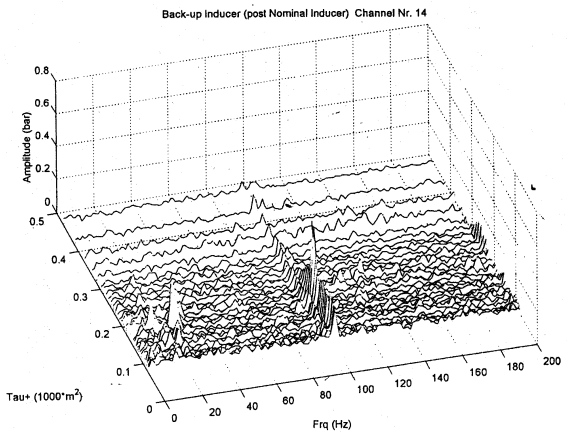

(d) Spectral pressure signal distribution for the final inducer configuration in water ($\dot{m} = \dot{m}_n$).

Figure 9: Experimental facilities in LOX and main results.

were exploited to reach this target. Mutual relationships were highlighted all along the development time activity. 3D fully–viscous computations allowed the designer to identify cavitation inception, and to compare performances of the reference and final inducer configurations. A parametric analysis of the performance was carried out by varying the leading edge shape, which is mainly responsible of rotating cavitation and induced radial loads. Both water and LOX tests assessed that the final modifications of leading edge shape are suitable to reduce rotating cavitation effects with a good smoothing of the ψ/τ curve, while preventing potentially dangerous excitations from being induced on the piping system.

Acknowledgments

The experimental activity which has led to results described in this work was performed as part of the *"Ariane 5"* cryogenic engine development program. This work was performed under FIAT Avio responsibility in the frame of the development of the *"Vulcain 2"* cryogenic engine, Snecma Moteurs as prime contractor under contracts of ESA/CNES. The authors would like to express their gratitude to FIAT Avio Management in Turin and Colleferro for their support; to ASTRIUM (Octobrunn site), which provided the experimental data for the complete pump in LOX; to Prof. Ennio Carnevale, Dean of Engineering at the University of Florence, for encouraging and promoting this joint research activity.

References

[1] Pervait, M., Garrett, J., and Kuvyla, J., "An Inducer CFD Solution and Effects Associated with Cavitation," *Workshop for CFD Application in Rocket Propulsion NASA–MSFC*, West Palm Beach, Florida, 1993.

[2] Pagnier, P., Morel, R., Spettel, F., Henry, C., and Champagne, J. Y., "Conception and Experimental Study of an Inducer," *Proceedings of the International Symposium on Cavitation CAV1995*, Deauville, France, May 1995.

[3] Kaenel, A. V., Morel, P., Maitre, T., Rebattet, C., and Kueny, J. L., "Three Dimensional Partial Cavitating Flow in a Rocket Turbopump Inducer: Numerical Predictions Compared with Laser Velocimetry Measurements," *Proceedings of the International Symposium on Cavitation CAV1995*, Deauville, France, May 1995.

[4] Zocco, A., Malagnino, G., Motta, M., and Munari, A., "Experimental Investigation on Radial Loads Induced by Partial Cavitation on LOX Turbopump of the "Ariane 5" Vulcain Engine," *Proceedings of the International Symposium on Cavitation CAV1995*, Deauville, France, May 1995.

[5] Chorin, A., "A Numerical Method for Solving Incompressible Viscous Flow Problems," *Journal of Computational Physics*, Vol. 2, 1967, pp. 12–26.

[6] Baldwin, B. S. and Lomax, H., "Thin layer approximation and algebraic model for separated turbulent flows," *AIAA paper*, Vol. 78, 1978, pp. 257.

[7] Arnone, A., Liou, M. S., and Povinelli, L. A., "Multigrid Calculation of Three-Dimensional Viscous Cascade Flows," *Journal of Propulsion and Power*, Vol. 9, No. 4, July-August 1993, pp. 605–614.

[8] Arnone, A., "Viscous Analysis of Three–Dimensional Rotor Flow Using a Multigrid Method," *Journal of Turbomachinery*, Vol. 116, July 1994, pp. 435–445.

[9] Arnone, A. and Pacciani, R., "Three-Dimensional Viscous Analysis of Centrifugal Impellers Using the Incompressible Navier-Stokes Equations," *1st European Conference on Turbomachinery - Fluid Dynamic and Thermodynamic Aspects*, Erlangen, March 1–3 1995, pp. 181–195.

[10] Arnone, A. and Benvenuti, E., "Three-Dimensional Navier-Stokes Analysis of a Two-Stage Gas Turbine," *ASME paper 94-GT-88*, 13-16 June 1994.

[11] Arnone, A., Boncinelli, P., Munari, A., and Spano, E., "Application of CFD techniques to the Design of the *Ariane 5* Turbopump," 14^{th} *AIAA Computational Fluid Dynamics Conference*, June 28 – July 1 Norfolk, VA 1999, pp. 1087–1097.

[12] Kamijo, K., Shimura, T., and Watanabe, M., "An Experimental Investigation of Cavitating Instability," *ASME 77-WA/FW14*, 1977.

[13] Brennen, C. E., *Hydrodynamics of Pumps*, Concepts ETI – Oxford University Press, 1994.

[14] Tsujimoto, Y., Kamijo, K., and Yoshida, Y., "A Theoretical Analysis of Rotating Cavitation Inducers," *ASME Journal of Fluid Engineering*, Vol. 115, 1993, pp. 135–141.

[15] Courtot, Y., Jousselin, F., and Reboud, J. L., “Cavitating Inducer Instabilities: Experimental Analysis and 2D Numerical Simulation of Unsteady Flow in Blade Cascade,” *Proceedings*, Fourth International Symposium on Cavitation CAV2001, Pasadena, California (USA), June 20–23 2001.

[16] Goirand, B., Mertz, A. L., Jousselin, F., and Rebattet, C., “Experimental Investigations of Radial Loads Induced by Partial Cavitation with a LH2 Inducer,” *Imech*, Vol. C453/056, 1992, pp. 263–269.

[17] Tsujimoto, Y., Yoshida, Y., Maekawa, Y., Waatanabe, S., and Hashimoto, T., “Observations of Oscillating Cavitation of an Inducer,” *ASME Journal of Fluid Engineering*, Vol. 119, 1997, pp. 775.